

3D/2D Projected Shape Sensitivity Analysis of Total Joint Arthroplasty Implants

Andrew James Jensen, Scott Banks, Ph.D.

Abstract

Recent advancements in computer vision and machine learning have facilitated fully autonomous kinematics measurement of Total Knee Arthroplasty (TKA) implant components. However, such performance has yet to be effectively replicated for Reverse Total Shoulder Arthroplasty (rTSA) implants. This study examines the correlation between 3D implant orientation and the sensitivity of their 2D projections, employing the Invariant Angular Radial Transform Descriptor (IARTD). It was observed that minor rotational differences along near-symmetric dimensions, such as the humeral internal-external rotation and the tibial internal/external axis, resulted in negligible shape alterations. Moreover, axes that posed challenges in registration were associated with reduced sensitivity of the descriptor. The findings indicate that symmetrical geometries and orientations inherently limit the amount of silhouette information that can be extracted. Nevertheless, the inclusion of bony anatomical landmarks as optimization constraints emerges as a promising approach to mitigate ambiguity and enhance registration accuracy.

Introduction

Understanding the in-vivo kinematics of total joint replacement has been essential in implant design, post-operative assessment, and predicting wear and failure patterns for nearly three decades [8, 4, 5]. Recent advancements in computer vision and machine learning have enabled these analyses for total knee arthroplasty (TKA) in a fully autonomous and clinically

practical setting, utilizing single-plane fluoroscopy [6, 9]. However, using only a single camera inherently limits the optimization due to loss of depth perception and the introduction of ambiguous projected shapes during optimization [7, 13, 21, 3]. The observed limitation, predominantly impacting mediolaterally symmetric tibial implants, led to a phenomenon termed “symmetry traps.” In such instances, two distinct three-dimensional orientations of the implant produce indistinguishable two-dimensional projected geometries. A machine learning algorithm was developed to address these symmetry traps. This algorithm was trained to recognize accurate anatomic orientations and correct images caught in optimization minima [10]. However, this approach required the symmetric implant to optimize into one of the two potential local minima, each corresponding to a distinct “symmetry trap.”

The application of the same optimization routine and cost function [7, 9] to reverse total shoulder arthroplasty (rTSA) resulted in significantly lower performance compared to its application in total knee arthroplasty implants. This suboptimal performance manifested in two primary ways. First, there was a consistent error along the internal/external rotation axis. This axis, characterized by near-rotational symmetry, frequently has features occluded by the glenosphere implant in frontal-plane fluoroscopy. Second, the optimization led to a distal shift of the implant. This shift meant that while the local minima correctly registered the humeral stem, they failed to do so for the humeral cup.

This pattern of failure prompted a deeper exploration into the perceptual psychology of shape [1, 2], underscoring the significance of high curvature as a salient feature in binary shapes. Additionally, binary distance metric studies [15, 16] emphasized the need to align the cost-function metric with the problem, considering the data’s underlying structure. In response to these new findings and to address the challenges identified with rTSA kinematics optimization, we developed two novel cost functions.

Menger’s discrete curvature algorithm [12] was applied to the projected implant’s contour to isolate keypoints of the highest curvature. Subsequently, a distance map (DM_k) for each keypoint was calculated, enabling rapid computation of Euclidean distances to these points. The high-curvature distance maps were then integrated into a *Modified Asymmetric Surface Distance*, focusing solely on the identified keypoints (Eq. 1). In this process, the minimum values from the element-wise multiplication of each distance map (DM_k) with the projection

estimate (p) were averaged. An error value of 0 would indicate a direct overlap of the estimated projection with all keypoints, confirming accurate registration in high-curvature regions. However, this approach, when applied to humeral implants, mirrored previously encountered errors, resulting in poor performance.

$$J = \frac{\sum_{k \in \mathbb{K}} (\min_{p \in Proj} (p \cdot DM_k))}{N}$$

where

\mathbb{K} = Set of all high-curvature keypoints (1)

N = Number of high-curvature keypoints

DM_k = Distance map for keypoint k

p = Single point on projection estimate

In response to the Modified Asymmetric Surface Distance cost function’s limitations, there was a shifted focus to refining the Hamming Distance [7, 9], especially due to its uniform error in non-overlapping scenarios between the estimate and target mask. To overcome this limitation, a *Modified Mean Surface Distance* was developed. This involved the element-wise multiplication of the projection estimate ($Proj_{x,y}$) with the global distance map of the target ($DM_{x,y}$) (Eq. 2). Similar to the *Modified Asymmetric Surface Distance*, this approach also led to poor results.

$$J = \frac{\sum_{(x,y) \in Image} Proj_{x,y} DM_{x,y}}{\sum_{(x,y) \in Image} Proj_{x,y}} \quad (2)$$

The current investigation delves into the fundamental shape aspects of each arthroplasty system, with a focus on developing a method for autonomously measuring rTSA kinematics from single-plane images. Central to this is the use of Invariant Shape Descriptors, particularly the Invariant Angular Radial Transform Descriptor (IARTD), which offers a mathematically robust approach to describe object shapes. These descriptors are immune to variations in scale, translation, or orientation [20], and are adept at quantifying the relative “nearness”, “farness”, and “uniqueness” of shapes as vector differences. Such properties are valuable for object categorization [17, 18, 19] and kinematics measurement [3], with IARTD’s

sensitivity to radial shape differences [11] being particularly beneficial for detailed contour analysis.

The focus of this analysis is on the sensitivity of projected 2D shapes, as depicted by IARTD, to changes in their 3D orientation. This is key to understanding the impact of subtle orientation variations on the projected shape, an aspect integral to shape-based optimization metrics. The ultimate aim is to highlight performance differences in autonomous kinematics measurements between TKA and rTSA implant systems. Additionally, the study seeks to identify areas where imaging methods can be improved to boost the algorithm’s performance.

Methods

Data Collection

For shape sensitivity analysis, representative 3D models of reverse total shoulder arthroplasty (rTSA) humeral and glenosphere implants, as well as total knee arthroplasty (TKA) femoral and tibial implants, were obtained from a manufacturer. The study focused on a single size for each implant type, as the scale of the shapes was normalized using an Invariant Shape Descriptor, rendering multiple sizes unnecessary for this analysis.

Image Generation

Each implant’s binary silhouette was rendered to a 1024×1024 image plane using an in-house CUDA camera model (CUDA Version 12.1) [14]. The model featured a 1000mm focal length and 0.3mm per pixel resolution. All programming tasks utilized an NVIDIA Quadro P2200 GPU.

Invariant Angular Radial Transform

The Invariant Angular Radial Transform Descriptor (IARTD) was selected for its radial direction sensitivity, enabling the detection of subtle contour changes in projected shapes [11]. This sensitivity allows us to address minor changes along the contour of the projected

98 shape, which is a desirable property for determining the minor changes in shape with respect
 99 to input orientation.

100 IARTD computation involves aggregating orthogonal basis components across the unit
 101 polar disk, forming a complex moment. Each basis function has an order (n) and a repetition
 102 (p). The order can be visualized as concentric rings on the polar disk, and the repetition as
 103 the count of slices partitioning the unit disk along θ . For these calculations, the image is
 104 normalized so that the center is at $(0, 0)$, and the four corners are at $(\pm 1, \pm 1)$.

105 Each angular radial transform (ART) coefficient is a complex double integral (Eq. 3)
 106 over the image in polar coordinates, $f(\rho, \theta)$ multiplied by the ART basis function, $V_{np}(\rho, \theta)$
 107 (Eq. 4).

$$F_{np} = \int_0^{2\pi} \int_0^1 f(\rho, \theta) V_{np}(\rho, \theta) \rho d\rho d\theta \quad (3)$$

$$V_{np}(\rho, \theta) = A_p(\theta) R_n(\rho) \quad (4)$$

108 The radial basis function includes a complex exponential, $A_p(\theta)$ (Eq. 5), ensuring rota-
 109 tional invariance, and a trigonometric transform, $R_p(\theta)$ (Eq. 6), to establish orthogonality.

$$A_p(\theta) = \frac{1}{2\pi} e^{jp\theta} \quad (5)$$

$$R_n(\rho) = \begin{cases} 1 & n = 0 \\ 2 \cos(\pi n \rho) & n \neq 0 \end{cases} \quad (6)$$

111 Phase correction is applied to each ART coefficient (Eq. 7, Eq. 8) to adjust for differences
 112 in in-plane rotation.

$$\phi'_{np} = \phi_{np} - \phi_{n,1} \quad (7)$$

$$F'_{np} = F_{np} e^{-jp\phi_{n,1}} \quad (8)$$

113 Subsequently, the final feature vector is formulated by the polar decomposition of each

114 coefficient at every order and repetition (Eq. 9). Values from the first two repetitions are
 115 excluded, as they do not provide significant information [11]. The complete IARTD fea-
 116 ture vector encompasses values of $n = 0, \dots, 3$ and $p = 0, \dots, 8$ per the original authors’
 117 suggestion [11].

$$IARTD = \{|F'_{np}|, \phi'_{np}\} \text{ where } n \geq 0, p \geq 2 \quad (9)$$

118 Shape Differences and Sensitivity

119 In order to quantify the overall change between shapes, a readily interpretable value must
 120 be established. To simplify notation, successive rotations are denoted as subscripts, with
 121 $R_z R_x R_y$ being represented as $R_{z,x,y}$. Similarly, the application of the IARTD equation to an
 122 implant at a specific input orientation $R_{z,x,y}$ is denoted as $IARTD(R_{z,x,y})$. Shape differences
 123 were calculated using the central difference equation on the IARTD vector produced from
 124 two different orientations. The grid of sampled orientations had extrema of $\pm 30^\circ$ with a step
 125 size of 5° for each of the x , y , and z axes. The “differences” along each axis were computed
 126 using a positive and negative rotation ($\pm\delta$) of 1 degree. Therefore, for every set of x, y, z
 127 rotations, three distinct shape differences are computed, one each for δ_x , δ_y , and δ_z (Eq. 10).

128 For notational brevity, we will condense the total equation to a single $\Delta S(\delta)$, (represent-
 129 ing $\Delta Shape$ for a differential rotation δ).

$$\Delta S(\delta)_{z,x,y} \equiv \frac{\partial IARTD(R_{z,x,y})}{\partial \delta} \propto IARTD(R_{z,x,y,+\delta}) - IARTD(R_{z,x,y,-\delta}) \quad (10)$$

$$\forall \delta \in \{\delta_x, \delta_y, \delta_z\}$$

130 The disparate scales of IARTD vector elements necessitate their standardization, ensuring
 131 a balanced assessment of global behavior without overemphasis on any individual element.
 132 Z-scaling provides a practical approach to standardizing each element relative to its distri-
 133 bution. After z-scaling, the Euclidean norm of each $S(\delta)_{z,x,y}$ is calculated to quantify the
 134 total shape change for a specific differential rotation (Eq. 11).

135 The final step takes advantage of two factors: first, that the in-plane rotations are the
 136 first in the Euler sequence (z -axis), and second, that this type of rotation does not affect

Table 1: Average projected-shape sensitivity values for each of the implant models.

Implant Type	Average $\mathbb{S}(\delta_x)$	Average $\mathbb{S}(\delta_y)$	Average $\mathbb{S}(\delta_z)$
Humeral	8.83	4.82	7.08
Glenosphere	6.37	6.22	4.86
Femoral	6.88	8.68	4.93
Tibial	9.0	5.52	3.72

the in-plane shape. For each x and y input rotation, an average is computed from values where x and y remain constant while z varies (Eq. 12). The final values are obtained from this equation, denoted by \mathbb{S} . Individual plots will be created for $\mathbb{S}_{x,y}$, corresponding to each differential rotation in x , y , and z , and for each of the four implant types. An analysis of these plots will be conducted to assess the performance of JTML optimization and to explore areas where optimization faces significant challenges.

$$\|S(\delta)_{z,x,y}\|_2 \quad (11)$$

$$\mathbb{S}(\delta)_{x,y} = \frac{\sum_z \|S(\delta)_{z,x,y}\|_2}{N} \quad (12)$$

Results

The humeral implant exhibited the lowest mean $\mathbb{S}(\delta_y)$ across all implant types (Fig. 1) (Table 1). This rotation represents the final rotation in our Euler rotation sequence (Z-X-Y) and captures the internal/external rotation of the humeral implant. Additionally, the surface plotted by the humeral shape sensitivity for all $\delta_{x,y,z}$ is much smoother than any of the other plots, demonstrating the relative lack of shape difference for a wide range of input orientations. Several plots showed regions with relatively low sensitivity. Specifically, the glenosphere's δ_y sensitivity along the $y = 0$ axis (Fig. 2) and the tibial implant's δ_y sensitivity along the $x = 0$ axis (Fig. 4). The femoral implant had the highest average sensitivity ($\frac{\mathbb{S}(\delta_x) + \mathbb{S}(\delta_y) + \mathbb{S}(\delta_z)}{3}$) among all implant types .

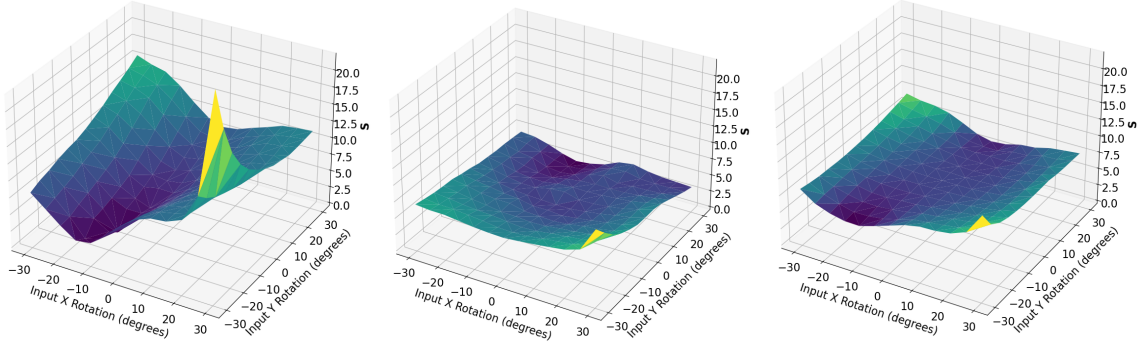


Figure 1: The \mathbb{S} plot for a humeral implant for δ rotations along the x, y, and z axis, respectively.

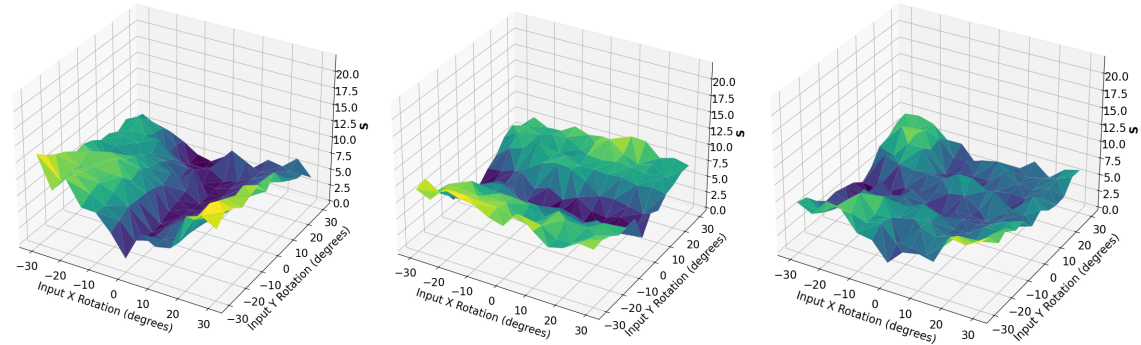


Figure 2: The \mathbb{S} plot for a glenosphere implant for δ rotations along the x, y, and z axis, respectively.

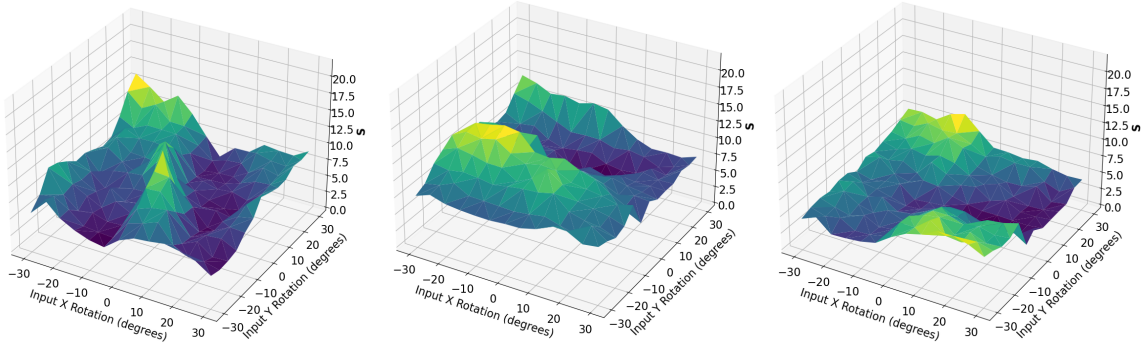


Figure 3: The \mathbb{S} plot for a femoral implant for δ rotations along the x, y, and z axis, respectively.

Discussion

The findings correspond closely with initial expectations regarding the sensitivity measurement of projected shapes relative to 3D object orientation and are consistent with areas

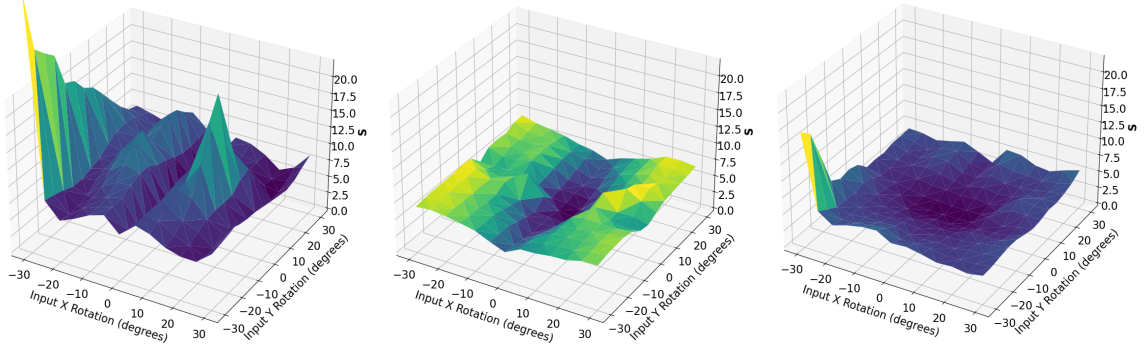


Figure 4: The \mathbb{S} plot for a tibial implant for δ rotations along the x, y, and z axis, respectively.

challenging for JTML optimization. Specifically, the humeral implant showed a generally smooth and minimal shape sensitivity profile, particularly for δ_y rotations (Table 1). Along this axis, the humeral implant is the most cylindrical, meaning we would not expect to see a significant change in the shape descriptor with minor δ_y rotations. Furthermore, it is noteworthy that this axis presented the most significant difficulties in JTML optimization.

Similar intuitive outcomes are observed with the glenosphere implant, which exhibited the lowest average $\mathbb{S}(\delta)$ among all the implant types. This implant primarily consists of an articulation surface closely approximating a spherical shape. Given that the projection of a sphere (a circle) remains constant regardless of the sphere’s orientation, the closer a shape is to a spherical form, the lower its overall shape sensitivity is expected to be.

The observed shape sensitivity of the tibial implant with respect to δ_y rotation aligns with the concept of symmetry traps. There is a consistently low shape sensitivity along the line where $x = 0$. This axis, associated with internal/external rotation, is the same one that contributes to symmetry traps, where two different 3D orientations result in an identical projected shape. In terms of this analysis, the ΔS value would be 0 for these two orientations of the tibial implant.

This study sheds light on an important aspect of Joint Track Machine Learning, particularly the use of Euler angles in the DIRECT-JTA optimization routine. Currently, the optimization does not involve independently varying all angles within a body-centered reference frame, as this approach is not conducive to hyperbox creation. Instead, optimization is performed over a range of ordered rotations, projected through the sequence $R_z R_x R_y$. The challenges the humeral implant encounters in aligning the y -axis illustrate that this ordered

sequence, especially with a symmetric final axis, can hinder the convergence process.

Beyond the inherent shape sensitivities, such optimization limitations motivate exploring alternatives to Euler angles. Performing registration optimization directly on the Special Orthogonal group $SO(3)$ poses an intriguing direction. $SO(3)$ encapsulates all possible 3D rotations in a mathematically convenient structure (A *Lie Group*, which is both a manifold and a group). By optimizing on this manifold instead of using specific angle parametrizations, issues with gimbal lock and cascade effects can be avoided. Optimization over Lie groups is an emerging subfield - establishing robust $SO(3)$ -based registration cost functions could significantly improve JTML convergence while relying less on descriptor sensitivity along certain axes.

Lastly, incorporating bone information into the optimization routine seems to be the most likely path forward for disambiguating difficult implant orientations. This study demonstrates that for specific implant geometries, there are inherent limitations to the information that can be gathered from the projected 2D shape as manifest in fluoroscopic imaging. Utilizing bone information, such as keypoints representing specific anatomic structures, would drastically increase the amount of information present during optimization, and could offer robust constraints on the possible 3D orientations of implant models.

Conclusion

This study demonstrates intrinsic differences between implant types regarding projected 2D shape sensitivity. Measurement difficulties aligned with low sensitivity along problematic axes—humeral internal rotation and tibial symmetry traps. Fundamentally, minor orientation changes yielded negligible 2D variability for near-symmetrical geometries. While inherent shape constraints limit data extractable solely from fluoroscopic silhouettes, incorporating additional image information like bone offers promise. Despite unavoidable ambiguity along select dimensions, boosting descriptor sensitivity and employing precise anatomical constraints could enable robust clinical tracking. Overall, relating optimization performance to shape response underscores routes toward accurate autonomous kinematic analysis.

References

- [1] Fred Attneave. “Some Informational Aspects of Visual Perception.” In: *Psychological Review* 61.3 (1954), pp. 183–193. ISSN: 1939-1471, 0033-295X. DOI: 10.1037/h0054663. URL: <http://doi.apa.org/getdoi.cfm?doi=10.1037/h0054663> (visited on 11/02/2023).
- [2] Fred Attneave and Malcolm D. Arnoult. “The Quantitative Study of Shape and Pattern Perception.” In: *Psychological Bulletin* 53.6 (Nov. 1956), pp. 452–471. ISSN: 1939-1455, 0033-2909. DOI: 10.1037/h0044049. URL: <http://doi.apa.org/getdoi.cfm?doi=10.1037/h0044049> (visited on 11/02/2023).
- [3] S.A. Banks and W.A. Hodge. “Accurate Measurement of Three-Dimensional Knee Replacement Kinematics Using Single-Plane Fluoroscopy”. In: *IEEE Transactions on Biomedical Engineering* 43.6 (June 1996), pp. 638–649. ISSN: 00189294. DOI: 10.1109/10.495283. pmid: 8987268. URL: <http://ieeexplore.ieee.org/document/495283/> (visited on 03/22/2021).
- [4] Scott A. Banks and W.Andrew Hodge. “2003 Hap Paul Award Paper of the International Society for Technology in Arthroplasty”. In: *The Journal of Arthroplasty* 19.7 (Oct. 2004), pp. 809–816. ISSN: 08835403. DOI: 10.1016/j.arth.2004.04.011. URL: <https://linkinghub.elsevier.com/retrieve/pii/S0883540304003067> (visited on 05/13/2021).
- [5] Scott A. Banks et al. “Rationale and Results for Fixed-Bearing Pivoting Designs in Total Knee Arthroplasty”. In: *The Journal of Knee Surgery* 32.07 (July 2019), pp. 590–595. ISSN: 1538-8506, 1938-2480. DOI: 10.1055/s-0039-1679924. URL: <http://www.thieme-connect.de/DOI/DOI?10.1055/s-0039-1679924> (visited on 10/19/2023).
- [6] Jordan S. Broberg et al. “Validation of a Machine Learning Technique for Segmentation and Pose Estimation in Single Plane Fluoroscopy”. In: *Journal of Orthopaedic Research* (Feb. 2023). ISSN: 0736-0266, 1554-527X. DOI: 10.1002/jor.25518. URL: <https://onlinelibrary.wiley.com/doi/10.1002/jor.25518> (visited on 02/13/2023).

- [7] P. D. L. Flood and Scott A. Banks. “Automated Registration of 3-D Knee Implant Models to Fluoroscopic Images Using Lipschitzian Optimization”. In: *IEEE Transactions on Medical Imaging* 37.1 (2018), pp. 326–335. DOI: 10.1109/tmi.2017.2773398.
- [8] Benjamin J. Fregly et al. “Computational Wear Prediction of a Total Knee Replacement from in Vivo Kinematics”. In: *Journal of Biomechanics* 38.2 (Feb. 2005), pp. 305–314. ISSN: 00219290. DOI: 10.1016/j.jbiomech.2004.02.013. URL: <https://linkinghub.elsevier.com/retrieve/pii/S0021929004000909> (visited on 08/05/2021).
- [9] Andrew J. Jensen et al. “Joint Track Machine Learning: An Autonomous Method of Measuring Total Knee Arthroplasty Kinematics From Single-Plane X-Ray Images”. In: *The Journal of Arthroplasty* 38.10 (May 2023), pp. 2068–2074. ISSN: 08835403. DOI: 10.1016/j.arth.2023.05.029. URL: <https://linkinghub.elsevier.com/retrieve/pii/S0883540323005521> (visited on 06/22/2023).
- [10] Andrew James Jensen et al. “Correcting Symmetric Implant Ambiguity in Measuring Total Knee Arthroplasty Kinematics from Single-Plane Fluoroscopy”. In: (In Review).
- [11] Jong-Min Lee and Whoi-Yul Kim. “A New Shape Description Method Using Angular Radial Transform”. In: *IEICE Transactions on Information and Systems* E95.D.6 (2012), pp. 1628–1635. ISSN: 0916-8532, 1745-1361. DOI: 10.1587/transinf.E95.D.1628. URL: https://www.jstage.jst.go.jp/article/transinf/E95.D/6/E95.D_1628/_article (visited on 11/21/2023).
- [12] J. C. Léger. *Menger Curvature and Rectifiability*. Apr. 30, 1999. arXiv: math/9905212. URL: <http://arxiv.org/abs/math/9905212> (visited on 01/10/2024). preprint.
- [13] M.R. Mahfouz et al. “A Robust Method for Registration of Three-Dimensional Knee Implant Models to Two-Dimensional Fluoroscopy Images”. In: *IEEE Transactions on Medical Imaging* 22.12 (Dec. 2003), pp. 1561–1574. ISSN: 0278-0062. DOI: 10.1109/TMI.2003.820027. pmid: 14649746. URL: <http://ieeexplore.ieee.org/document/1247785/> (visited on 03/22/2021).
- [14] John Nickolls et al. “Scalable Parallel Programming with CUDA”. In: *ACM Queue* 6.2 (Mar. 2008), pp. 40–53.

- [15] Annika Reinke et al. *Common Limitations of Image Processing Metrics: A Picture Story*. Aug. 15, 2023. arXiv: 2104.05642 [cs, eess]. URL: <http://arxiv.org/abs/2104.05642> (visited on 11/16/2023). preprint.
- [16] Annika Reinke et al. *Understanding Metric-Related Pitfalls in Image Analysis Validation*. Sept. 25, 2023. arXiv: 2302.01790 [cs]. URL: <http://arxiv.org/abs/2302.01790> (visited on 11/16/2023). preprint.
- [17] Charles W. Richard and Hooshang Hemami. "Identification of Three-Dimensional Objects Using Fourier Descriptors of the Boundary Curve". In: *IEEE Transactions on Systems, Man, and Cybernetics* SMC-4.4 (July 1974), pp. 371–378. ISSN: 0018-9472, 2168-2909. DOI: 10.1109/TSMC.1974.5408458. URL: <http://ieeexplore.ieee.org/document/5408458/> (visited on 10/25/2023).
- [18] Timothy P. Wallace and Owen R. Mitchell. "Analysis of Three-Dimensional Movement Using Fourier Descriptors". In: *IEEE Transactions on Pattern Analysis and Machine Intelligence* PAMI-2.6 (1980), pp. 583–588. ISSN: 0162-8828. DOI: 10.1109/TPAMI.1980.6447707. URL: <http://ieeexplore.ieee.org/document/6447707/> (visited on 03/04/2022).
- [19] Timothy P. Wallace and Paul A. Wintz. "An Efficient Three-Dimensional Aircraft Recognition Algorithm Using Normalized Fourier Descriptors". In: *Computer Graphics and Image Processing* 13.2 (Jan. 1980), pp. 99–126. ISSN: 0146664X. DOI: 10.1016/S0146-664X(80)80035-9. URL: <https://linkinghub.elsevier.com/retrieve/pii/S0146664X80800359> (visited on 03/04/2022).
- [20] Dengsheng Zhang and Guojun Lu. "Review of Shape Representation and Description Techniques". In: *Pattern Recognition* 37.1 (Jan. 1, 2004), pp. 1–19. DOI: 10.1016/j.patcog.2003.07.008.
- [21] S. Zuffi et al. "A Model-Based Method for the Reconstruction of Total Knee Replacement Kinematics". In: *IEEE Transactions on Medical Imaging* 18.10 (Oct./1999), pp. 981–991. ISSN: 02780062. DOI: 10.1109/42.811310. pmid: 10628957. URL: <http://ieeexplore.ieee.org/document/811310/> (visited on 09/01/2020).